

Revision 2-correction Dec. 27

Tin isotopes via fs-LA-MC-ICP-MS analysis record complex fluid evolution in single cassiterite crystals

Peng Liu¹, Jingwen Mao^{2*}, Bernd Lehmann^{3*}, Stefan Weyer⁴, Ingo Horn⁴, Ryan Mathur⁵,
Fangyue Wang⁶, Zhenhua Zhou²

¹ School of Earth Sciences and Resources, Chang'an University, Xi'an 710054, China

² Ministry of Natural Resources (MNR) Key Laboratory of Metallogeny and Mineral Assessment, Institute of Mineral Resources, Chinese Academy of Geological Sciences (CAGS), Beijing 100037, China

³ Mineral Resources, Clausthal University of Technology, 38678 Clausthal-Zellerfeld, Germany

⁴ Institut für Mineralogie, Leibniz Universität Hannover, 30167 Hannover, Germany

⁵ Juniata College, Huntingdon, PA 16652, USA

⁶ Ore Deposit and Exploration Centre, School of Resources and Environmental Engineering, Hefei University of Technology, Hefei 230009, China

Corresponding author:

Jingwen Mao: jingwenmao@263.net;

Bernd Lehmann: lehmann@min.tu-clausthal.de

23 **ABSTRACT**

24 Tin isotope geochemistry of cassiterite may allow for reconstructing the fluid evolution of tin
25 ore deposits. Here, we present cathodoluminescence (CL) imaging, trace element and
26 *in-situ* Sn isotope compositions of two cassiterite crystals from an early and a relatively late
27 stage of ore formation of the Xiling vein-style Sn deposit, southeastern China, by
28 femtosecond laser-ablation multi-collector inductively- coupled plasma mass spectrometry
29 (fs-LA-MC-ICP-MS). Our results show that the early-stage cassiterite from a
30 high-temperature feldspar-stable hydrothermal environment has core, mantle and rim zones
31 with a systematic decrease in $\delta^{124/117}\text{Sn}_{3161\text{A}}$ (relative to the Sn standard NIST 3161A) from
32 $+0.38 \pm 0.06 \text{‰}$ in the crystal core to $-0.12 \pm 0.06 \text{‰}$ (2 SE) in the mantle zone. This isotopic
33 evolution, also paralleled by a decrease in Ta content by two orders of magnitude, suggests
34 a fluid batch evolving towards isotopically lighter Sn. The very rim zone of this crystal has an
35 intermediate tin isotope composition at about $+0.05 \text{‰}$ $\delta^{124/117}\text{Sn}_{3161\text{A}}$, combined with
36 elevated Ta, suggestive of a second fluid batch. The late-stage cassiterite crystal from a
37 muscovite-stable hydrothermal environment has a core with an evolved Sn isotope
38 composition at about -0.15‰ $\delta^{124/117}\text{Sn}_{3161\text{A}}$ combined with low Ta, and a rim with heavier Sn
39 isotope compositions up to $+0.30 \pm 0.08 \text{‰}$ $\delta^{124/117}\text{Sn}_{3161\text{A}}$ and higher Ta contents. As for the
40 early-stage crystal, two different fluid batches must be involved in the formation of this
41 crystal. Our pilot study highlights the advantage of spatially resolved analysis compared to
42 conventional, solution Sn-isotope analysis of bulk cassiterite crystals. The Sn isotope
43 variations at the micro-scale reveal the complexity of cassiterite crystal growth by a
44 combination of closed- and open-system fluid evolution and isotope fractionation.

45 INTRODUCTION

46 Cassiterite [SnO₂] is the most important ore mineral in tin deposits and can form in
47 magmatic and hydrothermal systems over broad *P-T-X* conditions ([Jackson and Helgeson](#)
48 [1985a, b](#); [Heinrich 1990](#)). Individual cassiterite crystals commonly show distinct zonation
49 patterns in optical ([Cheng et al. 2019](#)), cathodoluminescence (CL) or backscatter images,
50 and corresponding microchemical features, indicating changes in physico-chemical
51 conditions during their growth process.

52 Tin has 10 stable isotopes and investigations of the Sn isotope composition
53 revealed ‰-level variations in natural materials, including meteorites ([Creech and Moynier](#)
54 [2019](#)) and Sn ore deposits ([Haustein et al. 2010](#); [Yamazaki et al. 2013](#), [Schulze et al. 2017](#);
55 [Yao et al. 2018](#)), and even more significant variations between magmatic rocks from the
56 Earth and the Moon ([X.Y. Wang et al. 2018, 2019](#)). The first MC-ICP-MS reconnaissance
57 studies by [Haustein et al. \(2010\)](#) and [Yamazaki et al. \(2013\)](#) observed significant differences
58 in tin isotope composition among cassiterite samples from different localities. The latter
59 study identified a range in $\delta^{124/120}\text{Sn}_{\text{SPEX}}$ of -0.44 to +0.38 (corresponding to $\delta^{124/120}\text{Sn}_{3161\text{A}}$ of
60 +0.11 to +0.93) in cassiterite from Eastern Asia. A similar range was also observed by
61 [Brügmann et al. \(2017\)](#) in cassiterite from European and Near East tin ore deposits. [Yao et](#)
62 [al. \(2018\)](#) showed that the tin isotope composition of cassiterite from global tin deposits (with
63 $\delta^{124/116}\text{Sn}_{3161\text{A}}$ of 0.48 ± 0.62 ‰, 1 sigma) is consistently less fractionated than
64 paragenetically later stannite [Cu₂FeSnS₄] formed at lower temperature (with -1.47 ± 0.54 ‰,
65 1 sigma). This isotopic shift has been attributed to the oxidation of Sn²⁺ in solution and
66 concomitant precipitation of heavy-Sn-enriched cassiterite (SnO₂ with Sn⁴⁺), resulting in

67 residual dissolved Sn with lighter isotopic composition, which is expressed in the more
68 negative $\delta^{124/115}\text{Sn}$ values of later-formed stannite. Theoretical and experimental studies
69 suggest that Sn isotope fractionation can be caused by redox reactions and liquid-vapor
70 phase separation (Polyakov et al. 2005; Wang et al. 2019; She et al. 2020). However,
71 previous empirical studies focused on Sn-isotope determinations of bulk samples by solution
72 chemistry and MC-ICP-MS analysis. Up to now, *in-situ* Sn isotope measurements were only
73 reported by Schulze et al. (2017), comparing solution MC-ICP-MS to *in-situ* measurements
74 using femtosecond laser-ablation multi-collector inductively-coupled mass spectrometry
75 (LA-MC-ICP-MS). Spatially resolved methods, including *in-situ* Sn-isotope analysis of
76 cassiterite, may provide high resolution details that would remain unrecognized in solution
77 isotope analysis of bulk minerals or rocks.

78 Here, we combine CL, trace element and *in-situ* Sn isotopes to track changing fluid
79 compositions, as recorded in concentrically zoned cassiterite crystals. We selected two
80 cassiterite crystals from the hydrothermal vein-style Xiling tin deposit, southeastern China.
81 Our results indicate compositional heterogeneity at the sub-mm scale in terms of trace
82 elements and tin isotope composition, which reveal a more complex fluid evolution than
83 expected by analytical bulk mineral techniques. The features of the tin isotope fractionation
84 can be attributed to fractional crystallization of cassiterite, both in relatively closed-system
85 and open-system environments.

86

87 **GEOLOGICAL BACKGROUND AND SAMPLES**

88 The hydrothermal vein-style Xiling tin deposit is located in eastern Guangdong Province,

89 southeastern China ([Supplemental Fig. S1](#); see additional information in the Appendix 1).
90 The tin mineralization is predominantly hosted in Upper Jurassic volcanic/subvolcanic
91 rhyolite ([Fig. 1](#)), and the U-Pb age of cassiterite of 146-147 Ma suggests a hidden granite
92 intrusion as the source of the hydrothermal system ([Liu et al. 2018, 2019](#)). There are two
93 main ore types in the Xiling deposit: 1) veins of cassiterite + feldspar ± quartz, 2) veins of
94 cassiterite + quartz ± muscovite ([Figs. 2A-D](#)). These two mineral assemblages represent
95 early-stage (I) cassiterite related to potassic alteration, and relatively late-stage (II)
96 cassiterite related to phyllic alteration. Two-phase aqueous fluid inclusions from stage 1
97 have a salinity around 15 wt% NaCl eq. and homogenization temperatures of 350-380°C,
98 while the two-phase aqueous fluid inclusions from stage 2 have a low salinity ≤5 wt.% NaCl
99 eq. and homogenization temperatures of 250-280°C ([Liu et al. 2019](#)). We selected two
100 cassiterite crystals, hereafter referred to as early-stage cassiterite and late-stage cassiterite
101 (samples 17XL05 and 14XL01, respectively), which were prepared as thick polished
102 sections for cathodoluminescence imaging, LA-ICP-MS trace-element (single-spot and
103 mapping) and *in-situ* Sn isotope analysis (see analytical method for SEM-CL and
104 trace-element analysis in Appendix 1). Early-stage cassiterite occurs mostly as stout
105 prismatic, euhedral to subhedral crystals, 3-10 mm across in feldspar-quartz veins ([Fig. 2C](#)).
106 Late-stage cassiterite is found as prismatic euhedral crystals that are 1 to 4 mm across, in
107 muscovite-bearing quartz veins ([Fig. 2D](#)).

108

109 Analytical method for Sn isotope analysis

110 In-situ cassiterite Sn isotope analyses of cassiterite were performed at the Leibniz

111 Universität Hannover (Germany) by using a MC-ICP-MS (Thermo-Finnigan Neptune Plus)
112 instrument connected to an in-house built femtosecond laser ablation system based on a
113 Solstice (Spectra Physics, USA) regenerative amplified femtosecond laser and an UP-XP
114 laser stage system for beam delivery (New Wave Research). Detailed information about the
115 laser system can be found in Horn and von Blanckenburg (2007) and Schulze et al. (2017).
116 Tin isotope analyses were performed as outlined in Schulze et al. (2017) (and using the
117 same instruments). As detailed in Schulze et al. (2017), mass bias was corrected in this
118 study by sample-standard bracketing using a rod of pure Sn (99.9% Sn) (Halsbrücke,
119 Germany) as bracketing standard. Furthermore, an Sb mass bias monitor was introduced by
120 solution nebulization. A potential mass interference from ^{124}Te on ^{124}Sn was monitored by
121 simultaneous analyses of ^{125}Te . As the cassiterite crystals investigated in this study, were
122 generally heterogeneous, it was not possible to determine a value for the precision or even
123 “accuracy” of the *in-situ* analyses, e.g. based on replicate analyses. The precision and
124 accuracy of the *in-situ* analyses, judged on agreement with solution analyses, was
125 previously determined by Schulze et al. (2017). They analyzed several cassiterite crystals
126 (which were previously homogenized by melting) by both solution MC-ICP-MS and
127 fs-LA-MC-ICP-MS. With this approach, they could determine a precision (for replicate Laser
128 spot analyses) and estimate an accuracy (more precisely, agreement with solution analyses)
129 of better than 0.1 ‰ (at 95 % confidence level). This precision is considered as overall
130 uncertainty for reported Sn isotope ratios in this study. Internal precisions of individual
131 analyses, as reported in Table 1 were generally < 0.1‰ (2 SE) and are also shown as error
132 bars in Figures 4 and 5. The Sn isotope compositions are given as variation in parts per mil

133 (‰), using the δ notation. They are initially determined as $\delta^{124/117}\text{Sn}$ values relative to the Sn
134 rod:

$$135 \quad \delta^{124/117}\text{Sn}_{\text{rod}} = \left\{ \left[\frac{(^{124}\text{Sn}/^{117}\text{Sn})_{\text{sample}}}{(^{124}\text{Sn}/^{117}\text{Sn})_{\text{Sn rod}}} \right] - 1 \right\} \times 1000$$

136 The Sn rod standard was measured after every 1-2 sample analyses for drift monitoring.
137 The isotope composition of the Sn rod is indistinguishable from that of the SPEX CertiPrep
138 CLSN2-2Y standard (Schulze et al. 2017). Yamazaki et al. (2013) and Brüggmann et al. (2017)
139 cross-calibrated Sn SPEX CertiPrep CLSN2-2Y relative to NIST 3161A and found:
140 $\delta^{124/117}\text{Sn}_{3161A} = \delta^{124/117}\text{Sn}_{\text{SPEX}} + 0.55$. Combining the calibration of our Sn rod relative to
141 SPEX (Schulze et al. 2017) and the calibration of SPEX relative to NIST 3161A (Yamazaki et
142 al. 2013) and Brüggmann et al. (2017), we converted all isotope compositions determined in
143 this study relative to Sn rod to delta values relative to NIST 3161A by applying the following
144 equation:

$$145 \quad \delta^{124/117}\text{Sn}_{3161A} = \delta^{124/117}\text{Sn}_{\text{rod}} + 0.55$$

146 We used this conversion to facilitate comparison to previously published values, e.g. for
147 Bulk Silicate Earth (Wang et al. 2018) and other studies on ores (Yao et al. 2018).

149 RESULTS

150 The images of optical microscopy, cathodoluminescence (CL) and tantalum
151 trace-element mapping of the two cassiterite crystals are presented in Figures 2E-H, and
152 complemented by Supplemental Figures S2 and S3. The complete list of LA trace-element
153 data is in Supplemental Tables S1 and S2. Some selected variation plots are in Figure 3 and
154 will be discussed below. Additional variation plots are in Supplemental Figure S4.

155 The Sn isotope results of the two cassiterite crystals are presented in Table 1, relative to
156 Sn rod = SPEX and also converted relative to NIST 3161A. The slope of $\delta^{124/117}\text{Sn}$ vs.
157 $\delta^{119/117}\text{Sn}$ is 3.6 with an $r^2=0.97$, very close to the terrestrial fractionation line with the slope of
158 3.5, indicating natural mass-dependent fractionation (Fig. 4). The 13 spot analyses on the
159 two cassiterite crystals gave $\delta^{124/117}\text{Sn}_{3161A}$ values varying from -0.18 ± 0.06 to $+0.38 \pm$
160 0.06 ‰ (2 SE). Figure 4 correlates the $\delta^{124/117}\text{Sn}$ data with the spot location relative to the
161 crystal cross-sections in Figures 2E-F.

162

163 DISCUSSION

164 Relationships between CL and trace-element zoning

165 The two cassiterite crystals have different zoning features, best visible in CL (Fig. 2):
166 Sample 17XL05 displays a dark core zone and a mantle zone with oscillatory zoning
167 between dominantly light zones, surrounded by a rim zone with two darker grey bands.
168 Sample 14XL01 has a dark to medium grey core zone and a rim zone with very fine-grained
169 muscovite inclusions which produce a sieve pattern of minute dark domains (muscovite) and
170 minute light grey domains (cassiterite) (Fig. 2D). This latter fabric could be related to
171 co-precipitation of muscovite and cassiterite as deduced from the optical image.

172 Sample 17XL05 displays negative correlations between Sn vs. Ti and Sn vs. Fe
173 (Supplemental Figs. S4A-B), and positive correlations between U vs. Ti, Ta vs. Nb, and V vs.
174 Sc (Fig. 3C, Supplemental Figs. S4C-4D). These correlations likely result from the various
175 known ionic substitutions in the cassiterite structure, i.e., Ti^{4+} , Zr^{4+} , $\text{U}^{4+} \rightarrow \text{Sn}^{4+}$, $\text{V}^{5+} + \text{Sc}^{3+} \rightarrow$
176 2Sn^{4+} , $\text{Fe}^{3+} + (\text{Nb}, \text{Ta})^{5+} \rightarrow 2\text{Sn}^{4+}$, $2(\text{Nb}, \text{Ta})^{5+} + (\text{Fe}, \text{Mn})^{2+} \rightarrow 3\text{Sn}^{4+}$, (Möller et al. 1988;

177 [Plimer et al. 1991](#); [Murciego et al. 1997](#); [Neiva 2008](#)), and will not be further discussed here.

178 The relationship of trace elements and CL features in cassiterite was discussed in Farmer et
179 al. ([1991](#)).

180 The Ta contents are all below <1000 ppm and indicate a hydrothermal environment
181 whereas Ta >1000 pm, and up to the percent range, characterizes cassiterite from the
182 transitional magmatic-hydrothermal stage, such as in rare-metal alkali-feldspar granite
183 ([Zoheir et al. 2020](#)) or from rare-metal pegmatites ([Tindle and Breaks 1998](#)). Tantalum is
184 largely insoluble in hydrothermal fluids which is why Ta deposits are all related to rare-metal
185 pegmatite systems, but not to hydrothermal systems. Nevertheless, hydrothermal cassiterite
186 carries Ta as a trace element which likely is controlled by fluid conditions (temperature and
187 composition) ([Fesser 1968](#); [Schneider et al. 1978](#); [Tindle and Breaks 1998](#); [Lukyanova et al.](#)
188 [2017](#); [Akinfiyev et al. 2020](#)). Zirconium is also an element largely immobile in acid fluid
189 systems such as in tin ore systems, and can be regarded as an indicator of fluid evolution,
190 similar to Ta ([Möller and Dulski 1983](#); [Lehmann 1990](#)). There are distinct differences
191 between the two crystals studied, with consistent trends ([Fig. 3](#)). Sample 17XL05 has a core
192 with elevated Ta (mean around 90 ppm Ta), which decreases outward rapidly down to about
193 1 ppm Ta in the mantle zone, while the rim zone is again rich in tantalum (mean around 167
194 ppm Ta). Sample 14XL01 has a core with very little Ta (≤ 1 ppm), and rim zone slightly
195 elevated with 4-17 ppm Ta. These trends are also seen in zirconium, where the core of
196 sample 17XL05 is again high (about 210 ppm Zr), the mantle zone is lower at about 90 ppm
197 (mean) Zr, and the rim zone again higher with around 210 ppm Zr. Sample 14XL01 has a
198 core with only about 1 ppm Zr, and rim zone with slightly elevated Zr (mean around 15 ppm).

199 The pattern of both elements can be understood as controlled by temperature and fluid
200 composition/evolution. The lower Ta and Zr contents in the core zone of sample 14XL01 are
201 likely related to a lower formation temperature of this cassiterite crystal in the muscovite vein
202 stage, and a corresponding change in fluid composition towards lower salinity. The overall
203 elevated Ta and Zr contents in the core zone of sample 17XL05 are related to the higher
204 temperature of formation in the feldspar stage and elevated salinity (and possibly also
205 fluoride activity which has a large control of Ta solubility; [Akinfiiev et al. 2020](#)). The internal
206 decrease in Zr and Ta in the mantle zone of this crystal indicates depletion of these two
207 elements in a closed system. Interestingly, the rim zones in both crystals show again an
208 increase in Ta and Zr, which suggests another fluid batch at elevated temperature. We will
209 show below that these trends correlate with the Sn isotope patterns.

210

211 **Insights from *in-situ* Sn isotopes of cassiterite**

212 The range of isotope ratios measured in the cassiterite crystals from Xiling, ~ -0.1 to
213 $\sim +0.4$ ‰ $\delta^{124/117}\text{Sn}_{3161\text{A}}$, is within the 5-permil-range reported for cassiterite samples
214 worldwide, such as those given in Yao et al. ([2018](#)) for the major tin provinces (Cornwall,
215 Erzgebirge, Bolivia), and St. Austell/Cornwall, Bangka/Indonesia and Viloco/Bolivia ([Schulze
216 et al. 2017](#)). The available data from South China correspond to the Xiling cassiterite, i.e.
217 $\delta^{124/117}\text{Sn}_{3161\text{A}}$ for Dulong at -0.22 ± 0.18 ‰ (2 SD) and Gejiu at $+0.22 \pm 0.19$ ‰ (2 SD),
218 recalculated from the original $\delta^{124/120}\text{Sn}_{\text{SPEX}}$ data ([Yamazaki et al. 2013](#)). Overall, these data
219 are close to Bulk Silicate Earth of 0 to $+0.2$ ‰ $\delta^{124/117}\text{Sn}_{3161\text{A}}$ as estimated by X.Y. Wang et al.
220 ([2018](#)), and suggest little fractionation during the igneous formation and granite-related

221 evolution of the magmatic-hydrothermal tin ore systems. However, the available data
222 indicate significant differences between different tin deposits and within these deposits. The
223 microanalytical in-situ data of single cassiterite crystals indicate isotope fractionation
224 processes within the hydrothermal (micro)-environment.

225 Seven spot analyses on cassiterite 17XL05 show $\delta^{124/117}\text{Sn}_{3161\text{A}}$ values varying from
226 -0.12 ± 0.06 to $+0.30 \pm 0.06$ ‰ (2 SE) (Fig. 5A). There is a narrow range of $\delta^{124/117}\text{Sn}$ ($+0.20$
227 to $+0.38$ ‰) values in the core zone with a little decrease from the core zone 1 to 2 (Fig. 5A).
228 This decrease correlates with a significant decrease in Ta content from ~ 100 ppm to ~ 10
229 ppm (Fig. 6). There is a distinct decrease from $+0.20$ to -12 ‰ $\delta^{124/117}\text{Sn}_{3161\text{A}}$ from the core to
230 mantle zone (Fig. 5A). The mantle zone has very little Ta on the order of <2 ppm. Thus, the
231 variation of $\delta^{124/117}\text{Sn}$ towards lighter Sn from the core to the mantle zones seems to
232 correlate with a systematic decrease in Ta. Both trends can be interpreted as fluid evolution
233 due to fractional crystallization with D (crystal/fluid) $\text{Ta} \gg 1$, and preferential incorporation of
234 heavy Sn isotopes into cassiterite. Alternatively, Sn isotopes could fractionate during
235 vapor-liquid phase separation (D. Wang et al. 2019; She et al. 2020). However, in the case
236 of Xiling, no low-salinity vapor fluid inclusions are observed, thus precluding the possibility of
237 Sn transport as gaseous species. Also, with respect to Ta, Xiling has no individual Ta
238 minerals, as expected according to the very low solubility of tantalum in aqueous fluids, and
239 Ta is essentially in high-temperature cassiterite. In fact, cassiterite is the only tin mineral
240 phase in the deposit sampled, and there is no stannite, which is known from other deposits
241 to have lighter Sn compared to cassiterite. The latter characteristic has been explained as a
242 result of redox-controlled Sn isotope fractionation, where heavy Sn is favored in cassiterite

243 during the oxidation from Sn²⁺ (fluid) to Sn⁴⁺ (cassiterite), which then shifts the remaining
244 fluid towards lighter composition in stannite (Yao et al. 2018). However, the same process
245 can also explain the trend of lighter Sn composition in a single cassiterite crystal in a closed
246 system (Polyakov et al. 2005).

247 Six spot analyses on cassiterite 14XL01 yield $\delta^{124/117}\text{Sn}_{3161\text{A}}$ values ranging from $-0.17 \pm$
248 0.10 to $+0.30 \pm 0.08$ ‰ (2 SE) (Fig. 5B). The four lower $\delta^{124/117}\text{Sn}$ values in the inner zone
249 are relatively uniform (-0.17 to -0.08 ‰), whereas the two $\delta^{124/117}\text{Sn}$ values in the outer zone
250 are higher and increase from $+0.11$ to $+0.30$ ‰ (Fig. 5B). The $\delta^{124/117}\text{Sn}$ in the inner zone is
251 similar to the mantle zone in sample 17XL05, whereas the Ta content is on the order of <1
252 ppm Ta. We interpret this situation as representing an advanced fluid evolution with respect
253 to the Sn isotope composition and Ta content. The outer zone of crystal 14XL01 is
254 characterized by very-fine-grained intergrowth of cassiterite and muscovite, as evidenced by
255 sporadically elevated contents in Al (or deficiency in Sn) measured via LA-ICP-MS. The
256 cassiterite has very variable but elevated Ta contents (Fig. 2H), and the isotope data
257 characterize a less evolved fluid compared to the inner zone (Fig. 6). Therefore, the rim zone
258 must relate to a second fluid batch with an isotope composition similar to the initial fluid (core
259 zone I) of crystal 17XL05, but of lower temperature as deduced from the relatively lower Ta
260 and Zr contents.

261

262 **IMPLICATIONS**

263 Trace element compositions in cassiterite have been frequently used to fingerprint the
264 fluid evolution of tin deposits. The new microanalytical technique of tin isotope tracing within

265 individual cassiterite crystals provides an additional means to better characterize the
266 multi-stage scenarios leading to tin ore formation. The single-spot tin isotope analysis
267 documents tin isotope fractionation trends and yields information of the fluid system at high
268 spatial (and by analogy: temporal) resolution. The *in-situ* Sn isotope results reveal variations
269 of Sn isotope composition through growth zones of single cassiterite crystals, which cannot
270 be retrieved from conventional, solution Sn-isotope analysis of bulk samples. The isotopic
271 trends in individual crystals show the interplay of fractional crystallization of the tin isotope
272 composition in both closed- and open-fluid systems. Hence, tin isotope patterns in
273 combination with trace-element microanalysis may help to better understand the complex
274 zoning patterns of cassiterite and its associated fluid evolution.

275

276 **ACKNOWLEDGMENTS**

277 Peng Liu thanks Alexandre Raphael Cabral, Wenlei Song and Chao Zhao for editorial
278 comments on an early version of this paper. We also thank Prof. Fangzhen Teng and
279 Hongwu Xu, and two anonymous reviewers for their corrections and constructive comments.
280 This research was jointly funded by the National Natural Science Foundation of China
281 Projects (41902072, 41820104010), the China Geological Survey Project
282 (DD20190166-2020-06), Outstanding Chinese and Foreign Youth Exchange Program of
283 China Association of Science and Technology (Peng Liu) and Fundamental Research Funds
284 for the Central Universities (300102279301, 300102279401).

285

286 **REFERENCES**

- 287 Akinfiyev, N.N., Korzhinskaya, V.S., Kotova, N.P., Redkin, A.F., Zotov, A.V. (2020) Niobium
288 and tantalum in hydrothermal fluids: Thermodynamic description of hydroxide and
289 hydroxofluoride complexes. *Geochimica et Cosmochimica Acta*, 280, 102-115.
- 290 Brüggmann, G., Berger, D., and Pernicka, E. (2017) Determination of the tin stable isotopic
291 composition in tin-bearing metals and minerals by MC-ICP-MS. *Geostandards and*
292 *Geoanalytical Research*, 41, 437-448.
- 293 Cheng, Y.B., Spandler, C., Kemp, A., Mao, J.W., Rush, B., Hu, Y., and Blake, K. (2019)
294 Controls on cassiterite (SnO₂) crystallization: Evidence from cathodoluminescence
295 trace-element chemistry, and geochronology at the Gejiu tin district. *American*
296 *Mineralogist*, 104, 118-129.
- 297 Creech, J.B., and Moynier, F. (2019) Tin and zinc stable isotope characterization of
298 chondrites and implications for early Solar System evolution. *Chemical Geology*, 511,
299 81-90.
- 300 Farmer, C.B., Searl, A., and Halls, C. (1991) Cathodoluminescence and growth of cassiterite
301 in the composite lodes at South Crofty Mine, Cornwall, England. *Mineralogical Magazine*,
302 55, 447-458.
- 303 Fesser, H. (1968) Spurenelemente in bolivianischen Zinnsteinen. *Geologisches Jahrbuch*,
304 85, 605-610.
- 305 Haustein, M., Gillis, C., and Pernicka, E. (2010) Tin isotopy-a new method for solving old
306 questions. *Archaeometry*, 52, 816-632.
- 307 Heinrich, C.A. (1990) The chemistry of hydrothermal tin (tungsten) ore deposition. *Economic*
308 *Geology*, 85, 457-481.
- 309 Horn, I., and von Blanckenburg, F. (2007) Investigation of elemental and isotopic

- 310 fractionation during 196 nm femtosecond laser ablation multiple collector inductively
311 coupled plasma mass spectrometry. *Spectrochimica Acta Part B*, 62, 410-422.
- 312 Jackson, K.J., and Helgeson, H.C. (1985a) Chemical and thermodynamic constraints on the
313 hydrothermal transport and deposition of tin: I. Calculation of the solubility of cassiterite at
314 high pressures and temperatures. *Geochimica et Cosmochimica Acta*, 49, 1-22.
- 315 Jackson, K.J., and Helgeson, H.C. (1985b) Chemical and thermodynamic constraints on the
316 hydrothermal transport and deposition of tin. II. Interpretation of phase relations in the
317 Southeast Asian tin belt. *Economic Geology*, 80, 1365-1378.
- 318 Lehmann, B. (1990) *Metallogeny of tin*. Springer, 211 p.
- 319 Liu, P., Mao, J.W., Santosh, M., Xu, L.G., Zhang, R.Q., and Jia, L.H. (2018) The Xiling Sn
320 deposit, eastern Guangdong Province, Southeast China: A new genetic model from
321 $^{40}\text{Ar}/^{39}\text{Ar}$ muscovite and U-Pb cassiterite and zircon geochronology. *Economic Geology*,
322 113, 511-530.
- 323 Liu, P., Mao, J.W., Jian, W., and Mathur, R. (2020) Fluid mixing leads to main-stage
324 cassiterite precipitation at the Xiling Sn polymetallic deposit, SE China: evidence from fluid
325 inclusions and multiple stable isotopes (H-O-S). *Mineralium Deposita*, 55, 1233-1246.
- 326 Lukyanova, E.V., Akinfiev, N.N., Zotov, A.V., Rass, I.T., Kotova, I.T., Korzhinskaya, V.S.
327 (2017) Niobium in hydrothermal systems related to alkali granites: Thermodynamic
328 description of hydroxide and hydroxofluoride complexes. *Geology of Ore Deposits* 59 (4),
329 305-314.
- 330 Möller, P., Dulski, P. (1983) Fractionation of Zr and Hf in cassiterite. *Chemical Geology*, 40,
331 1-12.
- 332 Möller, P., Dulski, P., Szacki, W., Malow, G., and Riedel, E. (1988) Substitution of tin in
333 cassiterite by tantalum, niobium, tungsten, iron and manganese. *Geochimica et*

- 334 Cosmochimica Acta, 52, 1497-1503.
- 335 Murciego, A., Sanchez, A.G., Dusausoy, Y., Pozas, J.M., and Ruck, R. (1997) Geochemistry
336 and EPR of cassiterite from the Iberian Hercynian Massif. Mineralogical Magazine, 61,
337 357-365.
- 338 Neiva, A.M.R. (2008) Geochemistry of cassiterite and wolframite from tin and tungsten
339 quartz veins in Portugal. Ore Geology Reviews, 33, 221-238.
- 340 Plimer, I.R., Lu, J., and Kleeman, J.D. (1991) Trace and rare earth elements in
341 cassiterite-sources of components for the tin deposits of the Mole Granite, Australia.
342 Mineralium Deposita, 26, 267-274.
- 343 Polyakov, V.B., Mineev, S.D., Clayton, R.N., Hu, G., and Mineev, K.S. (2005) Determination
344 of tin equilibrium isotope fractionation factors from synchrotron radiation experiments.
345 Geochimica et Cosmochimica Acta, 69, 5531-5536.
- 346 Schneider, H.-J., Dulski, P., Luck, J., Möller, P., Villalpando, A. (1978) Correlation of trace
347 element distribution in cassiterites and geotectonic position of their deposits in Bolivia.
348 Mineralium Deposita, 13, 119-122.
- 349 Schulze, M., Ziegerick, M., Horn, I., Weyer, S., and Vogt, C. (2017) Determination of tin
350 isotope ratios in cassiterite by femtosecond laser ablation multicollector inductively
351 coupled plasma mass spectrometry. Spectrochimica Acta Part B, 130, 26-34.
- 352 She, J.X., Wang, T.H., Liang, H.D., Muhtar, M.N., Li, W.Q., and Liu, X.D. (2020) Sn isotope
353 fractionation during volatilization of Sn (IV) chloride: Laboratory experiments and quantum
354 mechanical calculations. Geochimica et Cosmochimica Acta, 268, 184-202.
- 355 Tindle, A.G., and Breaks, F.W. (1998) Oxide minerals of the Separation Rapids rare-element

- 356 granitic pegmatite group, northwestern Ontario. *Canadian Mineralogist*, 36, 609-635.
- 357 Wang, D., Mathur, R., Powel, W., Godfrey, L., and Zheng, Y.Y. (2019) Experimental evidence
358 for fractionation of tin chlorides by redox and vapor mechanism. *Geochimica et*
359 *Cosmochimica Acta*, 250, 209-218.
- 360 Wang, X.Y., Amet, Q., Titoussi, C., and Bourdon, B. (2018) Tin isotope fractionation during
361 magmatic processes and the isotope composition of the bulk silicate Earth. *Geochimica et*
362 *Cosmochimica Acta*, 228, 320-335.
- 363 Wang, X.Y., Fitoussi, C., Bourdon, B., Fegley, B., Charnoz, S. (2019) Tin isotopes indicative
364 of liquid-vapour equilibration and separation in the Moon-forming disk. *Nature Geoscience*,
365 12, 1009-1019.
- 366 Yamazaki, E., Nakai, S.I., Yokoyama, T., Ishihara, S., and Tang, H.F. (2013) Tin isotope
367 analysis of cassiterites from Southeastern and Eastern Asia. *Geochemical Journal*, 47,
368 21-35.
- 369 Yao, J.M., Mathur, R., Powell, W., Lehmann, B., Tornos, F., Wilson, M., and Ruiz, J. (2018)
370 Sn-isotope fractionation as a record of hydrothermal redox reactions. *American*
371 *Mineralogist*, 103, 1591-1598.
- 372 Zoheir, B., Lehmann, B., Emam, A., Radwan, A., Zhang, R., Bain, W.M., Steele-MacInnis, M.,
373 and Nolte, N. (2000) Extreme fractionation and magmatic-hydrothermal transition in the
374 formation of Abu Dabbab rare-metal granite, Eastern Desert, Egypt. *Lithos*, 352-353,
375 105329.
- 376
- 377

378

379

380 **FIGURE CAPTIONS**

381 **Figure 1.** Geological map of the Xiling deposit (Liu et al., 2018). Ore bodies are projected to
382 the surface.

383

384 **Figure 2.** A and B. Photographs and CL image of the ores from Stage I (potassic; sample
385 17XL05) and II (phyllic; sample 14XL01). C and D. Photomicrographs of cassiterite from
386 Stage I and II under crossed polarized light. E and F. CL images of the two cassiterite
387 crystals; the boundary between core and rim zones is marked by a yellow line. G and H. Ta
388 elemental mapping of the two cassiterite crystals. Abbreviations: Ab=albite; Cst=cassiterite,
389 Ms=muscovite, Kfs=K-feldspar, Qtz=quartz.

390

391 **Figure 3.** Selected scatterplots of trace elements (LA-ICP-MS) in the two cassiterite
392 samples (upper row: Sample 17XL05; lower row: Sample 14XL01): A, B, and C. Sn vs. Ta,
393 Zr vs. Ta, and U vs. Ti plots of Sample 17XL05; D, E, and F. Sn vs. Ta, Zr vs. Ta, and U vs. Ti
394 plots of Sample 14XL01. The large range in Sn content in D is largely due to muscovite
395 micro-inclusions. Overall elevated Ta and Zr contents in sample 17XL05 are due to the
396 higher temperature of formation of this cassiterite crystal (B). This explanation also applies
397 to the Ti-U plots (C, F), where the ratio of Ti/U in the fluid for the rim zone is apparently
398 higher than for the core-mantle zones.

399

400 **Figure 4.** Mass dependence of the cassiterite Sn-isotope data.

401

402 **Figure 5.** Sn isotope variation of the two cassiterite crystals, determined *in situ* by
403 fs-LA-MC-ICP-MS, shown as $\delta^{124/117}\text{Sn}_{\text{rod}}$ relative to the bracketing standard Sn rod, which is
404 indistinguishable to SPEX CLSN2-2Y (left y axis) and also as $\delta^{124/117}\text{Sn}_{3161A}$ relative to the
405 NIST 3161A standard (right y axis, see text for details in conversion of the standards). Error
406 bars are 2 SE.

407

408 **Figure 6.** Correlation between $\delta^{124/117}\text{Sn}_{3161A}$ and Ta content (spot analysis) for the two
409 cassiterite crystals analyzed.

410

411 **TABLE CAPTIONS**

412 **Table 1:** fs-LA-MC-ICP-MS isotope data for the two cassiterite samples (‰).

413

414 **SUPPLEMENTAL MATERIALS**

415 **Appendix 1**

416 **Supplemental table S1**

417 **Supplemental table S2**

418 **Supplemental figures (S1-S4)**

419

420

Table 1: fs-LA-MC-ICP-MS isotope data for the two cassiterite samples (‰).

	Sample spot	$\delta^{124/117}\text{Sn}_{3161\text{A}}$	$\delta^{124/117}\text{Sn}_{\text{rod}}$	2 SE	$\delta^{119/117}\text{Sn}_{\text{rod}}$	2 SE
1	17XL0501	0.30	-0.25	0.06	-0.09	0.03
2	17XL0502	0.38	-0.17	0.06	-0.06	0.03
3	17XL0503	0.20	-0.35	0.06	-0.11	0.03
4	17XL0504	0.20	-0.35	0.06	-0.12	0.03
5	17XL0505	-0.12	-0.67	0.06	-0.20	0.03
6	17XL0506	0.04	-0.51	0.06	-0.16	0.03
7	17XL0507	0.14	-0.41	0.06	-0.13	0.03
8	14XL0106	-0.14	-0.69	0.06	-0.21	0.04
9	14XL0105	-0.18	-0.73	0.06	-0.22	0.04
10	14XL0104	-0.17	-0.72	0.10	-0.21	0.07
11	14XL0102	-0.08	-0.63	0.08	-0.19	0.04
12	14XL0101	0.11	-0.44	0.08	-0.14	0.05
13	14XL0103	0.30	-0.25	0.08	-0.12	0.04

Note. Convert isotope compositions determined in this study relative to Sn rod

to delta values relative to NIST 3161A. $\delta^{124/117}\text{Sn}_{3161\text{A}} = \delta^{124/117}\text{Sn}_{\text{rod}} + 0.55$.

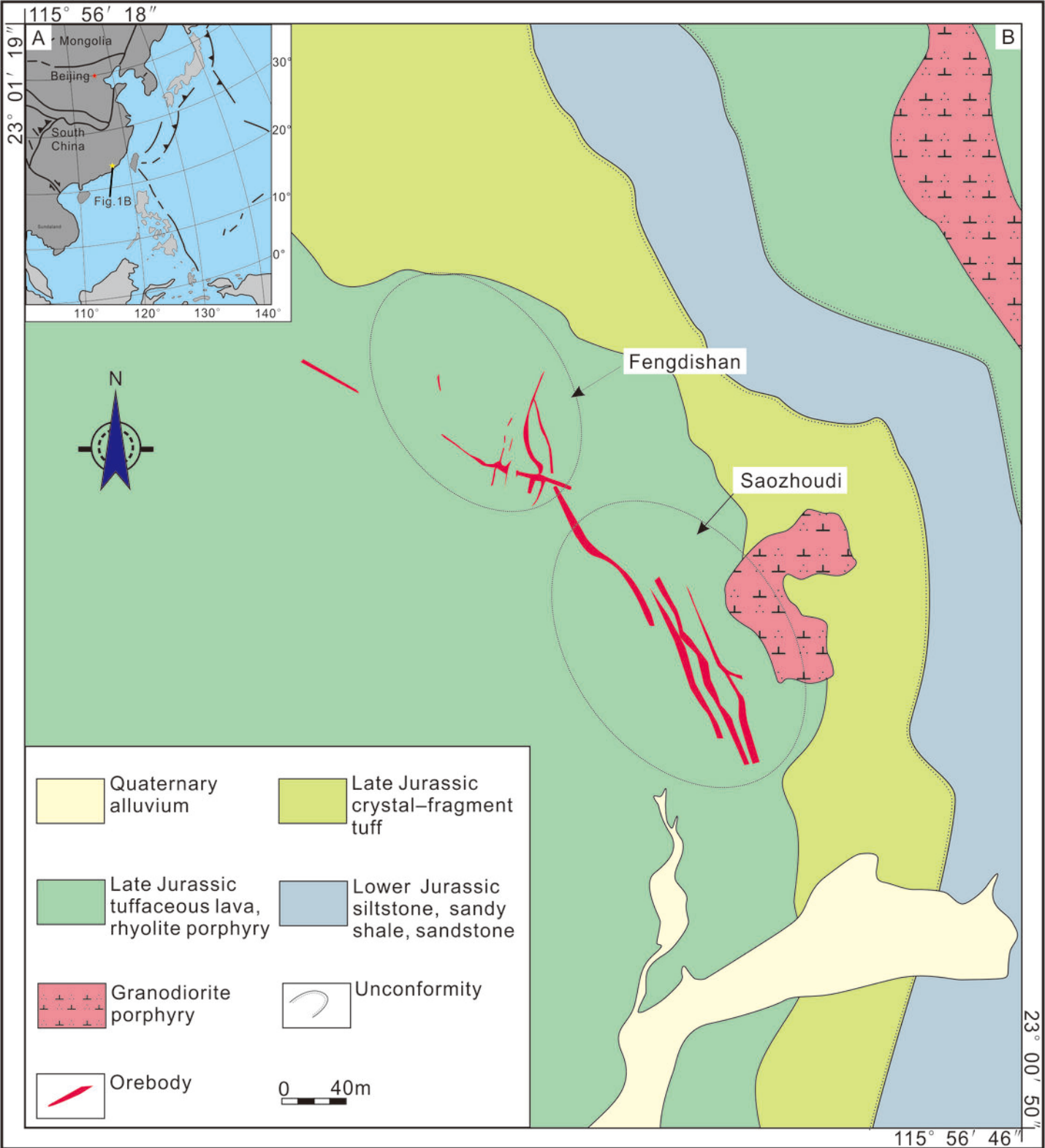


Fig. 1 (revision 2)

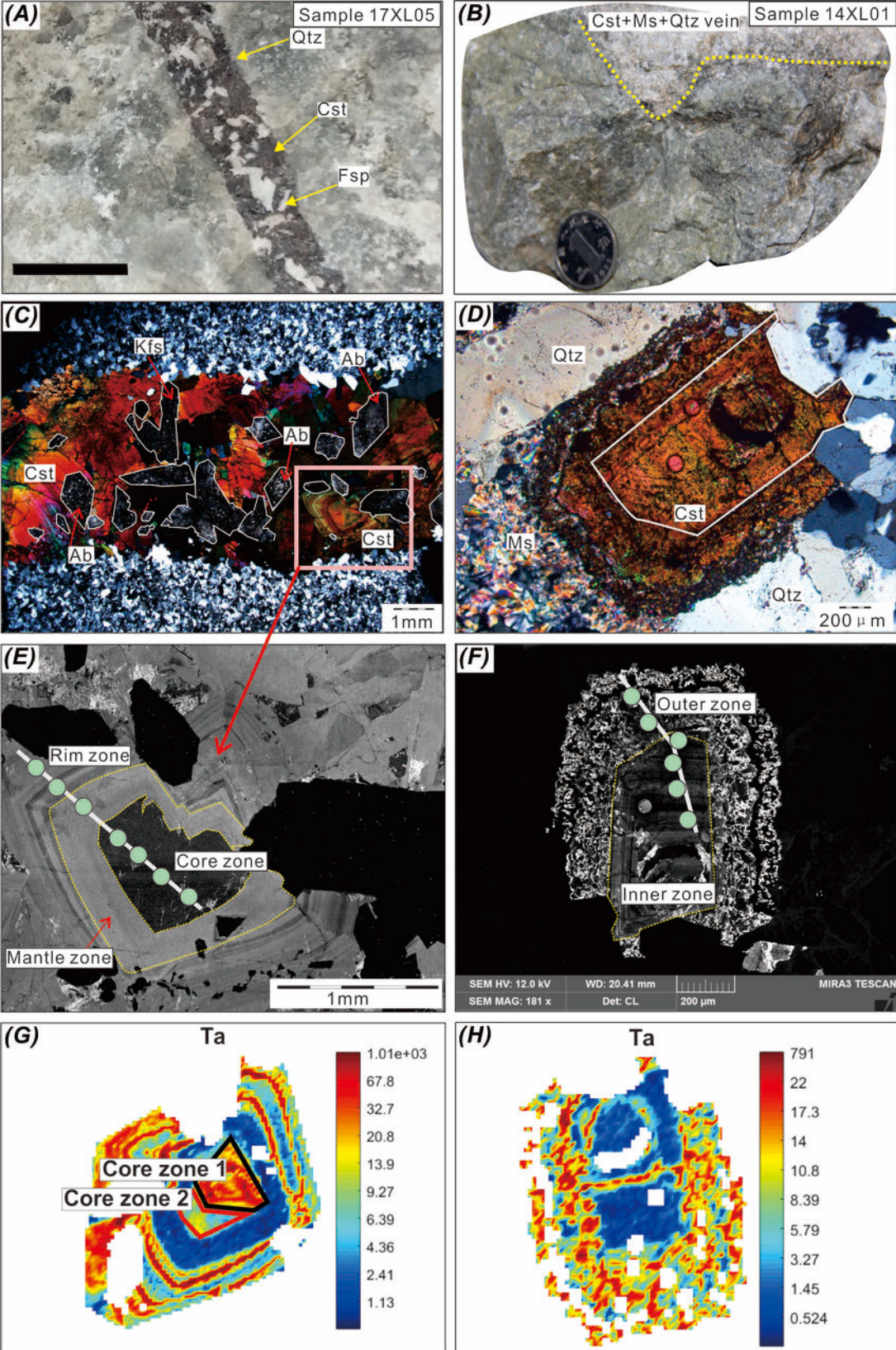


Fig.2 (revision 2)

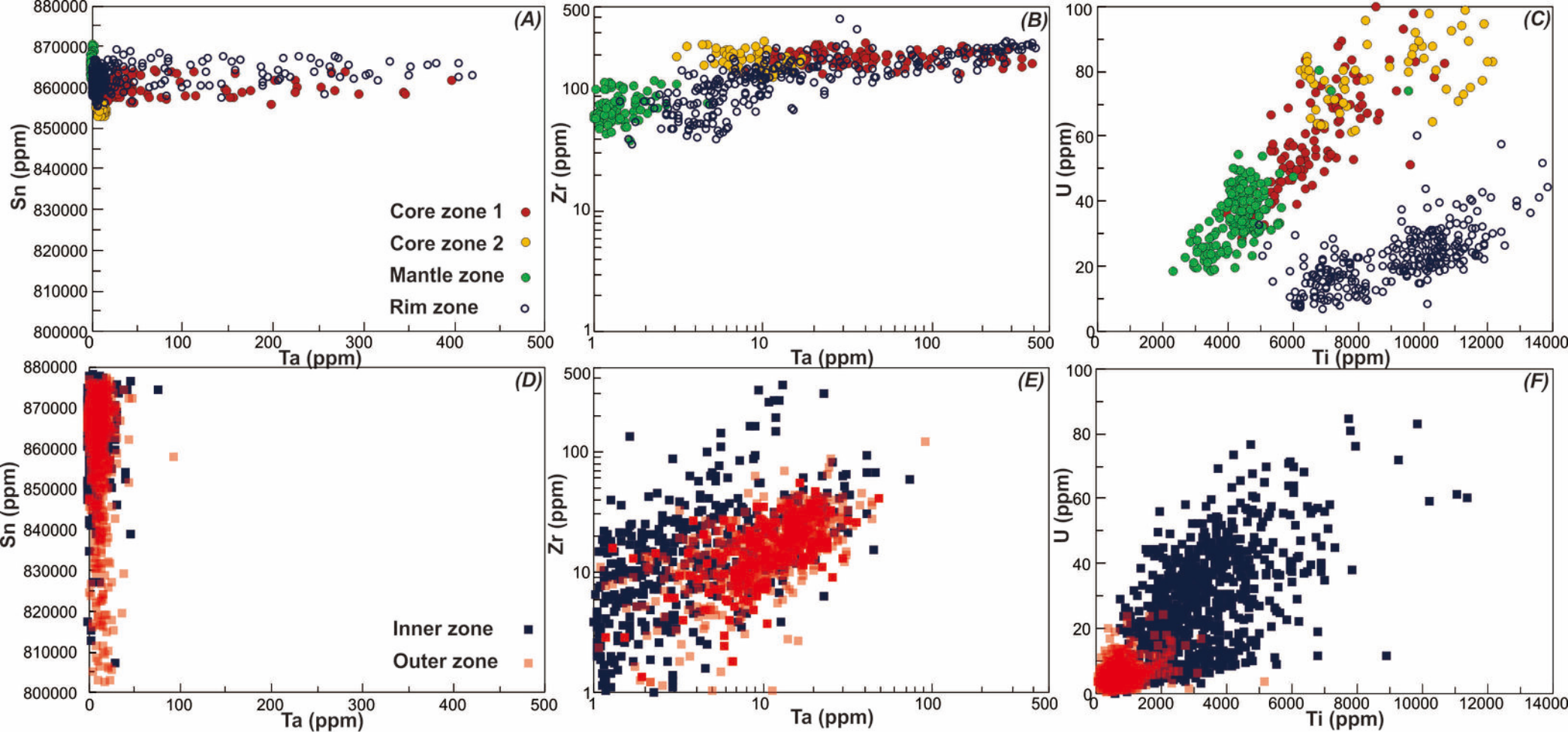


Fig. 3 (revision 2)

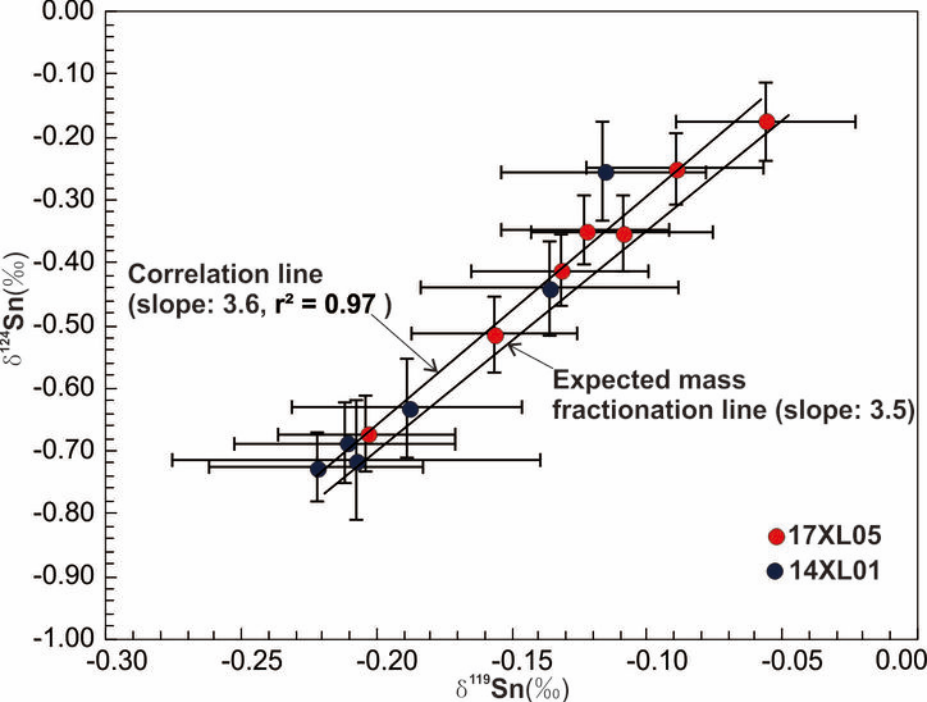


Fig. 4 (revision 2)

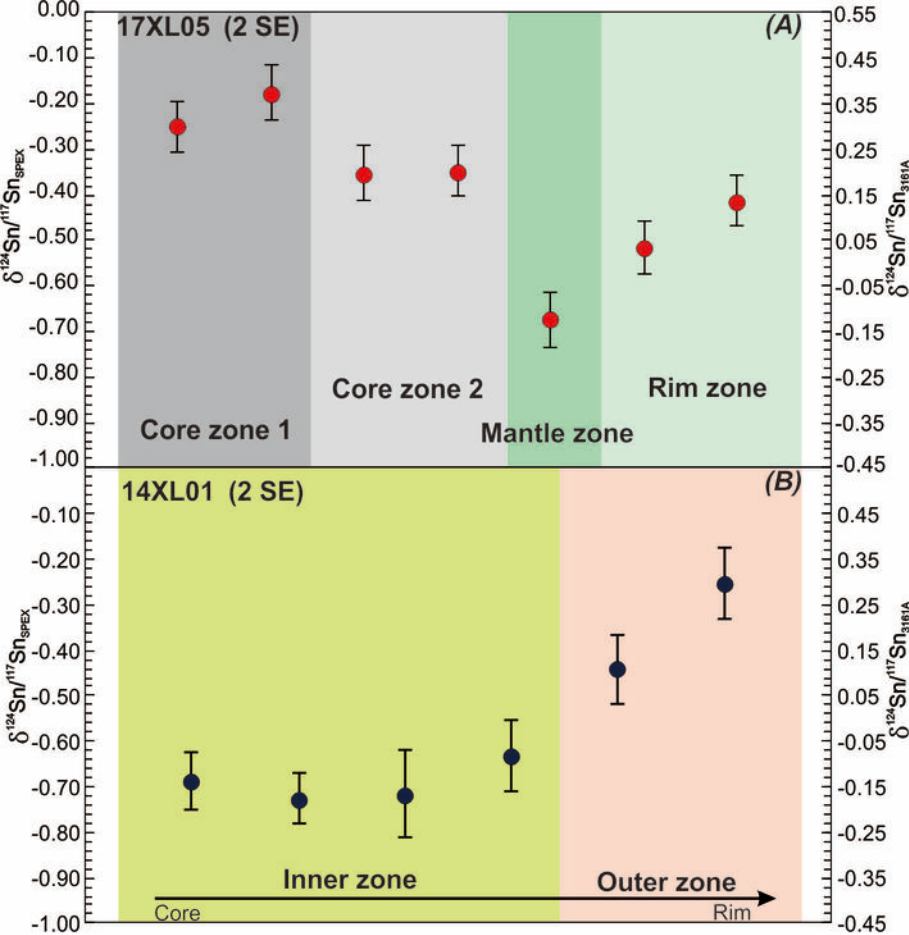


Fig. 5 (revision 2)

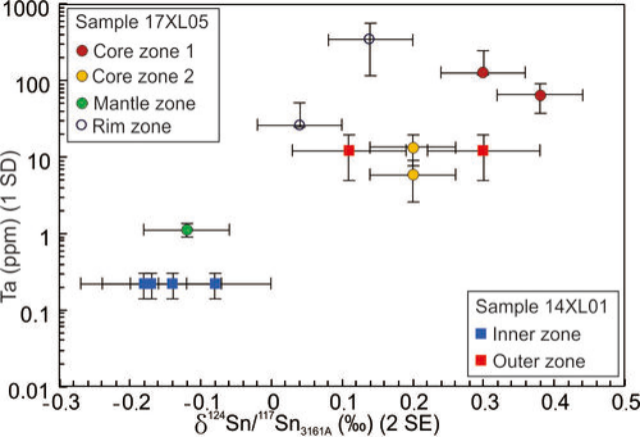


Fig. 6 (revision 2)